

## DENSITY PROFILES OF COLD DARK MATTER SUBSTRUCTURE: IMPLICATIONS FOR THE MISSING-SATELLITES PROBLEM

STELIOS KAZANTZIDIS<sup>1</sup>, LUCIO MAYER, CHIARA MASTROPIETRO, JÜRIG DIEMAND, JOACHIM STADEL, AND BEN MOORE

Institute for Theoretical Physics, University of Zürich, CH-8057 Zürich, Switzerland  
The Astrophysical Journal, accepted

### ABSTRACT

The structural evolution of substructure in cold dark matter (CDM) models is investigated combining “low-resolution” satellites from cosmological  $N$ -body simulations of parent halos with  $N = 10^7$  particles with high-resolution individual subhalos orbiting within a static host potential. We show that, as a result of mass loss, convergence in the central density profiles requires the initial satellites to be resolved with  $N = 10^7$  particles and parsec-scale force resolution. We find that the density profiles of substructure halos can be well fitted with a power-law central slope that is unmodified by tidal forces even after the tidal stripping of over 99% of the initial mass and an exponential cutoff in the outer parts. The solution to the missing-satellites problem advocated by Stoehr et al. in 2002 relied on the flattening of the dark matter halo central density cusps by gravitational tides, enabling the observed satellites to be embedded within dark halos with maximum circular velocities as large as  $60 \text{ km s}^{-1}$ . In contrast, our results suggest that tidal interactions do not provide the mechanism for associating the dwarf spheroidal satellites (dSphs) of the Milky Way with the most massive substructure halos expected in a CDM universe. Motivated by the structure of our stripped satellites, we compare the predicted velocity dispersion profiles of Fornax and Draco to observations, assuming that they are embedded in CDM halos. We demonstrate that models with isotropic and tangentially anisotropic velocity distributions for the stellar component fit the data only if the surrounding dark matter halos have maximum circular velocities in the range  $20 - 35 \text{ km s}^{-1}$ . If the dSphs are embedded within halos this large then the overabundance of satellites within the concordance  $\Lambda$ CDM cosmological model is significantly alleviated, but this still does not provide the entire solution.

*Subject headings:* cosmology: theory — dark matter — galaxies: halos — halos: evolution — halos: structure — methods:  $N$ -body simulations

### 1. INTRODUCTION

The concordance Lambda cold dark matter ( $\Lambda$ CDM) cosmological model for structure formation has been remarkably successful in explaining most of the properties of the universe on large scales and at various cosmic epochs. Recent results from microwave background experiments and large redshift surveys have highlighted the ability of this model to reproduce observations as diverse as the abundance and clustering of galaxies and clusters and the statistical properties of the  $\text{Ly}\alpha$  forest within constraints set by measurements of the primordial fluctuation spectrum, observations of distant Type Ia supernovae, and gravitational lensing statistics (e.g., Phillips et al. 2001; Jaffe et al. 2001; Percival et al. 2001; Hamilton & Tegmark 2002; Croft et al. 2002; Bahcall et al. 2003; Tonry et al. 2003; Spergel et al. 2003). However, on non-linear scales the  $\Lambda$ CDM model has been neither convincingly verified nor disproved, and several outstanding issues remain unresolved.

Specifically, the rotation curves of dwarf and low surface brightness galaxies are better fitted by shallower dark matter density profiles and lower concentrations than those predicted by the standard model (e.g., Flores & Primack 1994; Moore 1994; Burkert 1995; McGaugh & de Blok 1998; de Blok et al. 2001; de Blok, McGaugh, & Rubin 2001; de Blok & Bosma 2002; McGaugh, Barker, & de Blok 2003; Simon et al. 2003). However, cuspy dark matter distributions may be consistent with the rotation curve

data once systematic uncertainties are considered, such as non-circular motions due to the presence of a bar (Valenzuela & Klypin 2003; Rhee, Klypin, & Valenzuela 2003). Fast rotating bars require dark matter densities on galactic scales significantly lower than the theoretical predictions (Debattista & Sellwood 2000) and fluid dynamical models based on observations of barred galaxies support the same conclusion (Weiner, Sellwood, & Williams 2001). The inner Galaxy mass profile is marginally consistent with having dark matter in the central region (Binney & Evans 2001). On cluster scales, gravitational lensing observations are similarly suggestive of a discordance between the measured shallow dark matter density inner slopes and the predicted by numerical simulations cusps (Sand, Treu, & Ellis 2002; Sand et al. 2004). Nevertheless, hydrodynamical calculations of cluster formation have yet to be carried out and compared in detail with the observational data.

Among the most puzzling discrepancies on small scales is the so-called substructure problem.  $\Lambda$ CDM predicts a number of subhalos within the Local Group with maximum circular velocities in the range  $V_{\text{max}} \sim 10 - 30 \text{ km s}^{-1}$ , which is about 2 orders of magnitude higher than the total number of observed satellite galaxies (Kauffmann, White, & Guiderdoni 1993; Moore et al. 1999; Klypin et al. 1999). A number of possible solutions has been proposed to alleviate this problem. One class of solutions is related to radical modifications of the fundamental  $\Lambda$ CDM paradigm itself, including allowing for a finite dark matter particle self-interaction cross section that enhances the satellite destruction within galactic halos (Spergel &

<sup>1</sup> E-mail: stelios@physik.unizh.ch

Steinhardt 2000), reducing the small-scale power with a warm dark matter candidate (e.g., Avila-Reese et al. 2001; Eke, Navarro, & Steinmetz 2001; Bode, Ostriker, & Turok 2001), changing the shape of the primordial power spectrum (Kamionkowski & Liddle 2000; Zentner & Bullock 2002), introducing an interaction between dark matter particles and photons (Boehm et al. 2002) or resorting to the decay of a charged particle to suppress the small-scale power spectrum (Sigurdson & Kamionkowski 2003).

A second class of solutions relies on the inability of low mass satellites to form stars, by either supernova feedback, photoionization, or reionization. Indeed, baryon dissipation, star formation, and radiative feedback mechanisms must have a decisive effect on the properties of the final observed system, and it has been suggested that suppression of gas collapse and/or cooling by a photoionizing background at high redshift can dramatically reduce the number of visible satellites with  $V_{\text{vir}} < 50 \text{ km s}^{-1}$ , possibly reconciling the observations with the model predictions (Bullock, Kravtsov, & Weinberg 2000; Benson et al. 2002a,b). Nonetheless, these semi-analytical calculations adopt a simple description of the radiation physics and disagree with recent numerical simulations showing that even very small dwarf galaxies with circular velocities of the order of  $V_{\text{vir}} \sim 30 \text{ km s}^{-1}$  or even lower can self-shield themselves from the UV background and form some stars (Susa & Umemura 2003). Feedback processes may also violate the strong correlation between baryonic mass and virial velocity, as emphasized by Mayer & Moore (2003).

Recently, another way of relieving the missing satellites problem has been advocated by Stoehr et al. (2002, hereafter S02). These authors argue that the observed Galactic satellites are hosted by the most massive substructures within a given CDM halo. In this case, feedback processes suppress star formation in all smaller objects, and the “luminosity function” of the dwarf spheroidal galaxies (dSphs) is consistent with the “mass function” of the subhalos. This represents a somewhat simpler scenario than forming stars in a random 10% of the satellites over a larger mass range. However, in order to achieve this renormalization of the observed satellite mass/circular velocity function, S02 claimed that the observed velocity dispersions of the dSphs do not correlate with the maximum circular velocities,  $V_{\text{max}}$ , of their dark matter halos in the way originally assumed by Moore et al. (1999) and Klypin et al. (1999) when they identified the substructure problem.

As an illustrative example, consider the case of the dSph Fornax, with an observed stellar central velocity dispersion of  $\sigma_{\star} \sim 10 \text{ km s}^{-1}$  (Mateo 1998). The circular velocity of the surrounding dark matter halo at the location of the dwarf can be of the order of  $V_c = a\sigma_{\star} \sim 15 - 20 \text{ km s}^{-1}$ , depending on the particular assumptions made to infer such quantities from observations. For example, an isothermal halo model with a flat circular velocity profile, as adopted by Moore et al. (1999), would yield  $V_c = \sqrt{2}\sigma_{\star} = 14.1 \text{ km s}^{-1}$ . Provided that the circular velocity profile is still slowly rising in the region where the visible dwarf galaxy resides,  $V_c$  may substantially underestimate  $V_{\text{max}}$ . This would clearly allow the dwarf galaxies to be embedded in dark halos with very large maximum circular velocities in the range of  $V_{\text{max}} = 50 - 60 \text{ km s}^{-1}$ . However, such slowly rising circular velocity profiles seem

to be in notable disagreement with previous studies suggesting that the standard  $\Lambda$ CDM halos corresponding to the dSphs are expected to be very concentrated, which naturally leads to steeply rising circular velocity profiles (Bullock, Kravtsov, & Weinberg 2001).

S02 suggested that the satellites experience significant mass redistribution in their centers as a result of tidal interactions, leading to shallower inner density profiles and smaller effective concentrations than those of comparable isolated halos. However, the subhalos in their cosmological simulations contained just a few thousand particles and the softening lengths they used were comparable to the entire extent of some of the dSphs they wanted to resolve. These authors corroborated their results by comparing them with the higher resolution  $N$ -body simulations of Hayashi et al. (2003, hereafter H03), who employed individual cuspy model satellites disrupting in a static primary potential and found the same shallow inner density profiles as a result of tides. Nonetheless, the later models have the major shortcoming that they do not constitute equilibrium configurations, since they are constructed by approximating the exact velocity distribution at any given point in space with a Maxwellian. When evolved in isolation, these models relax rapidly to an inner density slope much shallower than the originally intended one, and any results obtained should be treated with care (Kazantzidis, Magorrian, & Moore 2004).

In this paper, we investigate how a satellite’s internal structure responds to tidal interactions, revisiting the solution to the missing-satellites problem proposed by S02. Our study uses  $N$ -body cosmological simulations of renormalized systems, in which the subhalos have up to 15 times more particles than those used by S02. Note, however, that Stoehr et al. (2003) confirmed the results of S02, using a simulation with a factor of 9 more particles. Furthermore, we investigate the tidal disruption of individual cuspy substructure halos, employing  $N = 10^7$  particles, 100 times the mass resolution of H03, to minimize numerical effects (Moore, Katz, & Lake 1996; Diemand et al. 2004a). Our primary goal is to examine the change in the internal structure of the substructure at scales comparable to the actual sizes of the luminous dwarf galaxies as they suffer tidal shocks and gravitational stripping. The models we adopt for the individual satellite simulations are self-consistent realizations and thus ideal for the sensitivity of this particular study. As we illustrate below, tides do not modify the central density structure of cuspy satellites and therefore the missing satellites problem can not be solved in this way.

This paper is organized as follows. In § 2, we discuss our cosmological and individual satellite simulations and present our results regarding the internal structural evolution of the substructure. In § 3, we model the kinematics of the Draco and Fornax dSphs on the basis of the findings of our simulations, and in § 4 we discuss the implications of our results. Finally, in § 5 we summarize our main findings and conclusions.

## 2. NUMERICAL SIMULATIONS

All the simulations carried out in this paper were performed with PKDGRAV (Stadel 2001), a multi-stepping, parallel,  $N$ -body tree code that uses a spline kernel soften-

ing such that the force is completely Keplerian at twice the quoted softening lengths. We used an adaptive, kick-drift-kick (KDK) leapfrog integrator, and the individual particle time-steps  $\Delta_t$  are chosen according to  $\Delta_t \leq \eta(\epsilon_i/\alpha_i)^{1/2}$ , where  $\epsilon_i$  is the gravitational softening length of each particle,  $\alpha_i$  is the value of the local acceleration, and  $\eta$  is a parameter that specifies the size of the individual time steps and, consequently, the time accuracy of the integration. The time integration conserved energy to better than 0.15% in all cases, which is adequate for the kind of numerical simulations presented in this paper. The energy must be conserved at such a level that the dynamics of the regions of interest can be meaningfully probed. We have also explicitly checked that our results are not compromised by choices of force-softening, time-stepping, or opening angle criteria in the treecode.

In what follows and unless otherwise explicitly stated, we consider as our framework the concordance flat  $\Lambda$ CDM cosmological model with present-day matter and vacuum densities  $\Omega_m = 0.3$  and  $\Omega_\Lambda = 0.7$ , respectively, dimensionless Hubble constant  $h = 0.7$ , present-day fluctuation amplitude  $\sigma_8 = 0.9$ , and index of the primordial power spectrum  $n = 1.0$ . Note also that in the remainder of this paper we use the terms “satellites,” “subhalos,” and “substructure” indistinguishably.

### 2.1. Substructure in a Fixed External Potential

In this section, we investigate the structural evolution of CDM substructure, using  $N$ -body simulations of satellites orbiting within the gravitational potential of a static primary. The satellites are modeled using the Navarro, Frenk, & White (1996, hereafter NFW) density profile, under the assumptions of spherical symmetry and isotropic velocity dispersion tensors. These models are constructed using the procedure described in Kazantzidis et al. (2004), which produces self-consistent equilibria that do not suffer from numerical instabilities present in other schemes, such as those that approximate the exact velocity distribution at any given point in space by a Gaussian.

The NFW density profile is given by

$$\rho(r) = \frac{\rho_s}{(r/r_s)(1+r/r_s)^2} \quad (r \leq r_{\text{vir}}), \quad (1)$$

where the characteristic inner density  $\rho_s$  and scale radius  $r_s$ , are sensitive to the epoch of halo formation and tightly correlated with the halo virial parameters, via the concentration,  $c \equiv r_{\text{vir}}/r_s$ , and the virial overdensity,  $\Delta_{\text{vir}}$ . Since the NFW density profile corresponds to a cumulative mass distribution that diverges as  $r \rightarrow \infty$ , we introduce an exponential cutoff for  $r > r_{\text{vir}}$ . The latter sets in at the virial radius and turns off the profile on a scale  $r_{\text{decay}}$ , which is a free parameter and controls the sharpness of the transition:

$$\rho(r) = \frac{\rho_s}{c(1+c)^2} \left(\frac{r}{r_{\text{vir}}}\right)^\epsilon \exp\left(-\frac{r-r_{\text{vir}}}{r_{\text{decay}}}\right) \quad (r > r_{\text{vir}}). \quad (2)$$

In order to ensure a smooth transition between equations (1) and (2) at  $r_{\text{vir}}$ , we require the logarithmic slope there to be continuous. This implies

$$\epsilon = -\frac{1+3c}{1+c} + \frac{r_{\text{vir}}}{r_{\text{decay}}}. \quad (3)$$

The satellites’ virial mass is equal to  $M_{\text{sat}} = 1.4 \times 10^{10} h^{-1} M_\odot$ , corresponding to a circular velocity at the

virial radius of  $V_{\text{vir}} = 35 \text{ km s}^{-1}$  for the adopted  $\Lambda$ CDM model. However, a dark matter halo of a given mass and size does not have a unique NFW profile. Indeed, the parameter that controls the shape of the density profile is the concentration  $c$ , and higher values of concentration correspond to a larger fraction of the virial mass being contained in the inner regions of the halo. For a given mass, the measured scatter in this parameter reflects mainly the different formation epochs (Bullock et al. 2001a; Eke, Navarro, & Steinmetz 2001; Wechsler et al. 2002). For the adopted  $\Lambda$ CDM model, the median concentration value for an object of this mass scale is  $c_{\text{sat}} = 21$ , with the  $2\sigma$  deviation given by  $c_{\text{sat}} \sim 11 - 40$  (Bullock et al. 2001a).

Here we present results for two high-resolution simulations ( $N = 10^7$ ) of subhalos having concentration parameters equal to  $c_{\text{sat}} = 21$  (HR1) and  $c_{\text{sat}} = 9$  (HR2). We consider these two significantly different values of the concentration to single out readily how the evolution of the satellites’ structure depends on this parameter. We note that values as small as  $c_{\text{sat}} = 9$  for the mass scale of our satellites are possible within models with a lower fluctuation amplitude  $\sigma_8$ . In order to demonstrate the need for such a high mass resolution, we run a simulation using a lower resolution of  $N = 5 \times 10^5$  particles with the lower value of the concentration  $c_{\text{sat}} = 9$  (LR). We emphasize that even the latter run uses a factor of 5 more particles than the highest-resolution simulations of H03.

For the low resolution run, we choose a spline softening length of  $\epsilon = 0.511h^{-1} \text{ kpc}$ . This value corresponds to an equivalent Plummer softening length equal to that of the highest resolution cosmological simulation, GA2, of S02. For models HR1 and HR2, we choose a gravitational softening of  $\epsilon = 0.021h^{-1} \text{ kpc}$ , comfortably smaller than the typical sizes of the dSph satellites of the Milky Way which constitute the ultimate target of the present study. Numerical and structural parameters of all models are summarized in Table 1. For all the runs, we followed the time evolution of the density,  $\rho(r)$ , and circular velocity,  $V_c(r)$ , profiles of the satellites. We explore below how these evolve depending on the structural properties of the subhalos and on the numerical resolution.

The orbits of the satellites are influenced only by the external, spherically symmetric static tidal field, which is represented by the logarithmic halo potential,

$$\Phi = \sigma^2 \ln(R^2 + R_c^2), \quad (4)$$

where  $\sigma$  is the one dimensional velocity dispersion and  $R_c$  is the core radius. We use  $\sigma = 127.3 \text{ km s}^{-1}$  and  $R_c = 0.7h^{-1} \text{ kpc}$ , resulting in a circular velocity profile that flattens out already at  $\sim 3 \text{ kpc}$  and reaches an asymptotic value of  $v_0 = \sqrt{2}\sigma \sim 180 \text{ km s}^{-1}$ . This modeling gives a total mass within 100 kpc of the center of the fixed potential equal to  $M_{R<100 \text{ kpc}} = 5.25 \times 10^{11} h^{-1} M_\odot$ . This value is at the upper limit of estimates for the mass of the Milky Way from satellite motions (Kochanek 1996) and dynamics of the Magellanic Clouds (Lin, Jones, & Klemola 1995), and it is within the range of models for the Milky Way proposed in the context of  $\Lambda$ CDM (Klypin, Zhao, & Somerville 2002). This choice serves our primary aim, which is to investigate the change of the satellites’ internal structure in a regime in which the tidal shocks are very strong. Note also that the total mass within the pericenter of the orbit is equal to  $M_{R<25 \text{ kpc}} = 1.3 \times 10^{11} h^{-1} M_\odot$ .

TABLE 1  
STRUCTURAL AND NUMERICAL PARAMETERS OF THE SATELLITE MODELS

| Model | $N$             | $c$ | $r_s$<br>( $h^{-1}$ kpc) | $V_{\text{peak}}$<br>( $\text{km s}^{-1}$ ) | $r_{\text{peak}}$<br>( $h^{-1}$ kpc) | $\epsilon_{\text{sat}}$<br>( $h^{-1}$ kpc) |
|-------|-----------------|-----|--------------------------|---|--------------------------------------|--|
| (1)   | (2)             | (3) | (4)                      | (5)   | (6)                                  | (7)  |
| LR    | $5 \times 10^5$ | 9   | 5.4                      | 41.5  | 11.7                                 | 0.511                                      |
| HR1   | $10^7$          | 21  | 2.3                      | 51.3  | 5.0                                  | 0.021                                      |
| HR2   | $10^7$          | 9   | 5.4                      | 41.5  | 11.7                                 | 0.021                                      |

Note. — Col. (1): Satellite galaxy model. Col. (2): Number of particles. Col. (3): Concentration parameter. Col. (4): Scale radius. Col. (5): Maximum circular velocity. Col. (6): Radius where the circular velocity peaks. Col. (7): Softening length. Note that the virial mass of all satellite models is  $M_{\text{sat}} = 1.4 \times 10^{10} h^{-1} M_{\odot}$ .

The orbits of the Milky Way dSphs are currently poorly constrained observationally. Nevertheless, their current distances, which give an indication of the apocenter of their orbits, coupled with studies of the orbital properties of cosmological halos, can be used to constrain the orbital parameters of the satellites. In particular, the model satellites are placed on an eccentric orbit with an apocenter radius of  $r_{\text{apo}} = 105h^{-1}$  kpc and  $(r_{\text{apo}}/r_{\text{per}}) = (6/1)$ , close to the median ratio of apocentric to pericentric radii found in high resolution cosmological  $N$ -body simulations (Ghigna et al. 1998; Tormen, Diaferio, & Syer 1998). The center of the external potential is always set to be  $(x, y, z) = (0, 0, 0)$ . We begin all our simulations by placing the satellites at apocenter, and we integrate the orbits forward for 7 Gyr. This timescale corresponds to more than three orbital periods ( $T_{\text{orb}} \sim 2.25$  Gyr) in the chosen orbit and already represents a significant fraction of the cosmic time. Our approach neglects the effects of the dynamical friction and the response of the primary to the presence of the satellite. However, this choice is justified given the difference in the mass (almost a factor of 50) and size of the two systems and the anticipated rapid and substantial mass loss owing to tides (see also Taffoni et al. 2003).

The tidal field alters the structure of the satellites through a combination of strong tidal shocks occurring at each pericentric passage and gradual mass loss throughout the orbital evolution. In the top panels of Figures 1 and 2, we present the evolution of the density (*left*) and circular velocity (*right*) profiles of the bound remnant of the initial models HR1 and HR2, respectively. After allowing the satellites to pass past the pericenter for the first time, we show the profiles at every odd quarter of the orbit between apocenter and pericenter. These profiles are plotted from the force resolution ( $2\epsilon$ ) outward. The choice of how to determine the bound remnants' center is crucial for our intended analysis, since quantities such as the spherically averaged density and circular velocity profiles are quite sensitive to the center's definition. In this study, we identify the center adopting the most bound particle method,

which agrees very well with the center of mass recursively calculated using spherical regions of decreasing radius. Indeed, we confirmed that both methods give converging results by comparing the resulting density profiles for some of our stripped satellites. This comparison yielded identical profiles for the remnants at all radii between our force resolution and the tidal radius for all the cases we tried.

We determine the mass that remains self-bound as a function of time using the following iterative scheme: in the rest frame of the most bound particle, we calculate the binding energies of all the other particles, using the tree-based gravity calculation performed by PKDGRAV, and we remove all those with positive binding energy. This calculation of binding energies and subsequent removal of unbound particles is repeated until no more particles can be removed or no bound remnant is found (i.e., all particles are removed). In practice, this iterative procedure converges rapidly and ensures that the true bound entity will be identified. Note that this technique is essentially the same one used by most group finding algorithms, such as the publicly available SKID (Stadel 2001), which we use for the substructure in the cosmological simulations analyzed in § 2.2, where removing the background potential is more difficult, but it has the advantages of (1) using a tree structure for the potential calculation which requires of the order of  $O(N \log N)$  operations instead of  $O(N^2)$ , where  $N$  is the number of particles in the remnant, and (2) having a parallel implementation for very large  $N$ . In this way, we can handle a much larger number of particles than would be possible with SKID, and at a fraction of the computational burden.

In the above analysis, we used equal-size logarithmic bins. Different number of bins were used, depending on the stage of the orbital evolution, ensuring that in each case we have a sufficiently large number ( $> 1000$ ) of particles in each bin. This choice of binning simply minimizes the noise in the resulting profiles. The central density of model HR2 decreases between the initial and final values by almost a factor of 3 more than the decrease in model HR1 over the same timescales. This is due to the fact that

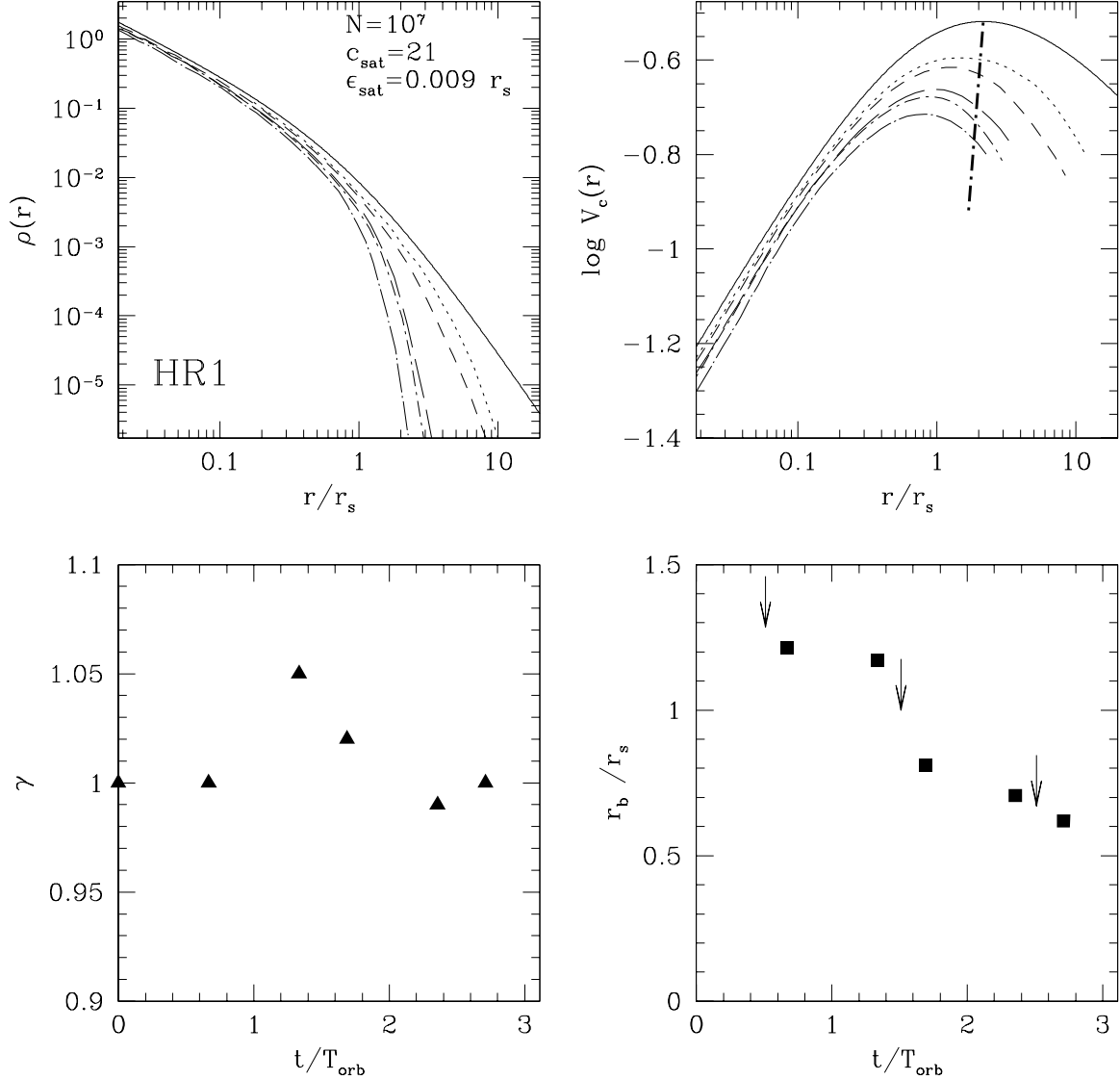


FIG. 1.— *Top:* Evolution of the density (*left*) and circular velocity (*right*) profiles of the bound mass for the high resolution model HR1. The number of particles,  $N$ , the concentration parameter,  $c_{\text{sat}}$ , and the softening length,  $\epsilon$ , are indicated (*upper right-hand corner*). The scale radius of this model is  $r_s = 2.3h^{-1}$  kpc. The orbital evolution shown corresponds to approximately three orbital periods ( $T_{\text{orb}} \sim 2.25$  Gyr). Profiles are shown at every odd quarter of the orbit between apocenter and pericenter, after allowing the satellites to pass the first pericenter, and are plotted from the force resolution ( $2\epsilon$ ) outward. The lines from top to the bottom, in order of decreasing central density, show the profiles at  $t = (0, 0.67, 1.33, 1.69, 2.36, 2.71) T_{\text{orb}}$ . The density and circular velocity are given in units of  $M_{\text{sat}}/r_s^3$  and  $(GM_{\text{sat}}/r_s)^{1/2}$ , respectively. The thick dotted line indicates the expected relation between  $V_{\max}$  and  $r_{\max}$  for field halos (see text for details). *Bottom:* Evolution of the central density slope  $\gamma$  (*left*) and break radius  $r_b$  (*right*) of the fitting formula (eq. [5]) that describes the structure of our subhalos. The latter fit parameter is expressed in units of the scale radius,  $r_s$ , of the initial model. Downward arrows indicate the pericentric passages. The substructures maintain the same steep central density slope down to the limit of our force resolution as they get tidally stripped. Tides, however, shift inward the break radius  $r_b$  of the fitting function. Note the considerable change in  $r_b$  after each pericentric passage.

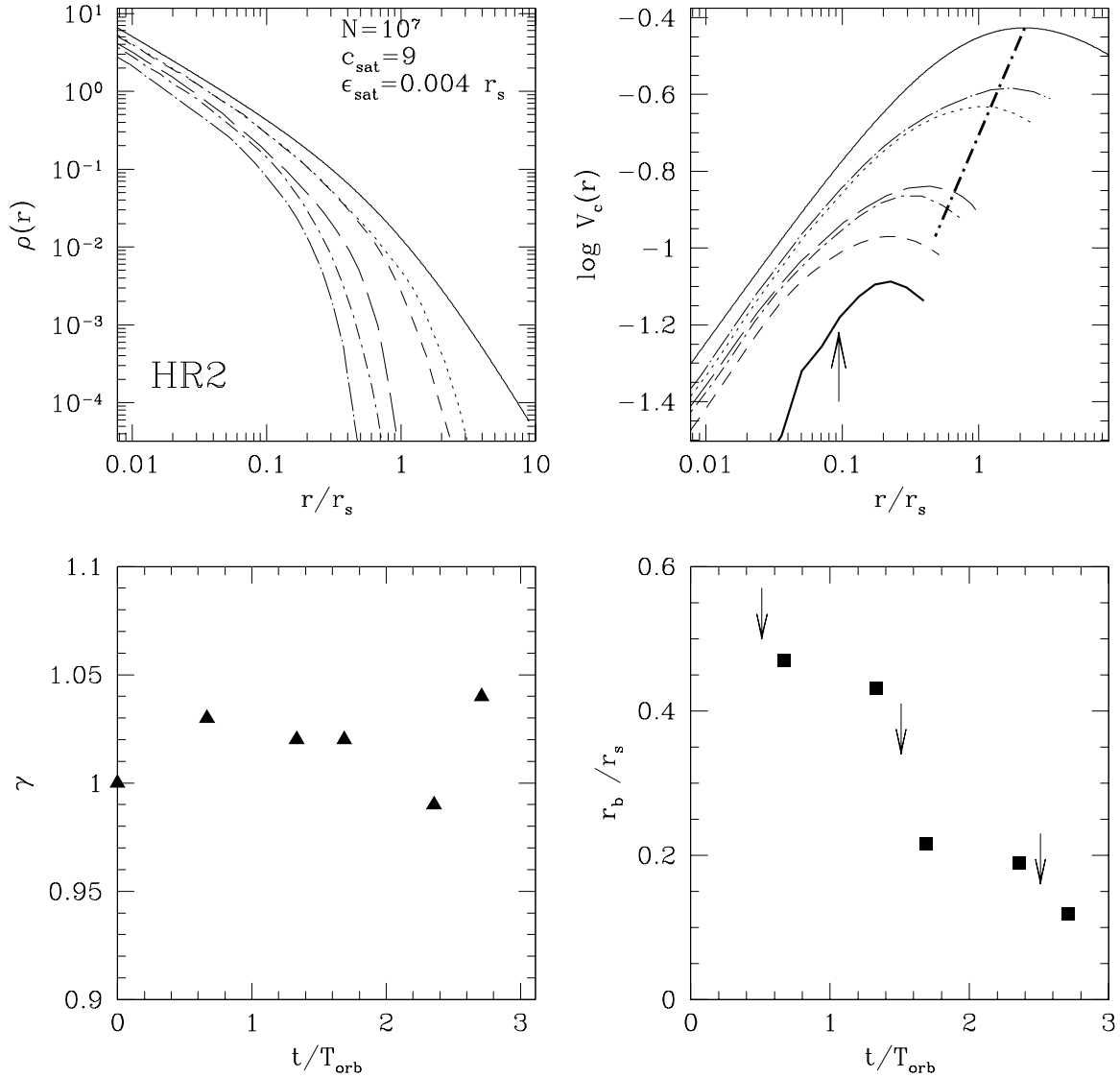


FIG. 2.— Same as Figure 1, but for model HR2. The scale radius is  $r_s = 5.4h^{-1}$  kpc. Compared to model HR1, the decrease in the central density and maximum circular velocity,  $V_{\text{max}}$ , is significantly more pronounced, because of the higher binding energy for more concentrated models. Tidal interactions truncate this model at smaller physical radii than in model HR1, which is reflected in the evolution of the break radius (*bottom right*). The thick solid line shows the circular velocity profile of the low resolution satellite (LR) at  $t = 2.71 T_{\text{orb}}$ . Even though this timescale is the same as the one corresponding to the last curve in the high-resolution run, the low resolution satellite has lost substantially more mass, and its central slope indicates a shallower inner density profile. Upward arrow indicates the softening used in the low resolution simulation.

the initial concentrations are quite different. The concentration parameter of model HR1 is considerably higher than that of HR2, and thus the former model is more resilient to tidal heating. The same effect is clearly seen on the evolution of the circular velocity profiles. In particular, the overall change in the  $V_{\max}$  is significantly more pronounced in model HR2 than in model HR1 for the same timescales. The thick dotted lines in the top right panels of Figures 1 and 2 indicate the expected relation between  $V_{\max}$  and the distance at which the maximum circular velocity,  $r_{\max}$ , occurs for *field halos* (Colin et al. 2003). The latter is a measure of the concentration of the satellites. Tidal stripping moves the subhalos to the left of the expected relation, so that for a given  $V_{\max}$  these systems have smaller  $r_{\max}$  and hence higher effective concentrations than field halos. For example, after  $\sim 6$  Gyr the  $V_{\max}$  and  $r_{\max}$  of the  $c_{\text{sat}} = 9$  satellite decrease by a factor of 3.5 and 8.5, respectively. For the same change of  $V_{\max}$ , however, one would expect  $r_{\max}$  to vary by just a factor of 3 from the relation for field halos. The higher relative densities of heavily stripped halos may account for the fact that Draco, being considerably closer to the Milky Way, has a mass-to-light ratio higher than that of Fornax, despite their similar stellar velocity dispersions.

The density structure of our subhalos can be described through the following simple formula

$$\rho(r) \propto r^{-\gamma} \exp\left(-\frac{r}{r_b}\right), \quad (5)$$

where  $\gamma$  denotes the central slope of the substructure density profile and  $r_b$  an effective “break” radius describing the outer cutoff imposed by the tides. In the bottom panels of Figures 1 and 2, we show the evolution of these two fitting parameters. Note that  $r_b$  is expressed in units of the scale radius,  $r_s$ , of the initial models. The robustness of the aforementioned binning procedure was verified by comparing these results against those when the particles were binned in spherical shells with the same number of particles in each bin. In this case, we choose as bin center the average radius of all particles in the given bin, and we assign equal statistical weight to each radial bin. The two procedures yielded almost identical values for  $\gamma$  and  $r_b$  for the entire orbital evolution. Note that in the bottom panels of Figures 1 and 2, we present our results adopting the latter binning procedure, and the same is also true for results shown in Figure 3.

The bottom left panels of Figures 1 and 2 demonstrate that tidal effects do not serve to reduce the central density cusp down to the limit of our force resolution. This is a fundamental result of this paper that is independent of the concentration of the satellites and valid for their entire orbital evolution. Most of the tidally stripped mass is removed from the outer parts of the subhalos, steepening the outer density profiles and shifting the break radius  $r_b$  inward. This just reflects the fact that tides truncate the satellite models at increasingly smaller physical radii. The two bottom right panels illustrate that the lower concentration satellite (HR2) gets truncated at smaller radii than its higher concentration counterpart. In both models, the break radii experience the biggest decrease after each pericentric passage, but this decrease is more pronounced in model HR2. Between pericenters the break radii decrease in a smoother manner.

Even though this result is also verified in the lower resolution model LR when we compared the density profiles, it is interesting to note that the same is not true for the circular velocity profiles. Indeed, convergence in the latter profile is significantly more problematic, and this is highlighted in the top right panel of Figure 2, where the circular velocity profile of the low resolution satellite is shown for comparison at  $t = 2.71 T_{\text{orb}}$  (*thick solid line*). The downward arrow indicates the softening used in this simulation. The circular velocity profile of a model satellite having a factor of 20 fewer particles than its high-resolution counterpart and evolved on the same orbit is significantly lower and has a steeper inner gradient. This is entirely due to resolution effects. The fact that the convergence in the circular velocity is harder to attain is not surprising, since it is a cumulative quantity (see also below, § 2.2). This warns against using the circular velocity to compute the structural properties of satellites, as done in S02.

Figures 1 and 2 indicate that the inner satellite regions corresponding to sub-kiloparsec scales are much less affected by the tides than the outer ones. In particular, the satellite with  $c_{\text{sat}} = 21$  suffers almost no change, even in the value of the central density. Subhalo particles that have orbital times shorter than the shock duration will be only marginally affected by the shock itself. This is known as adiabatic correction (Weinberg 1995). Especially for the satellite with the highest central density ( $c_{\text{sat}} = 21$ ), the adiabatic correction to the impulse approximation is extremely important, as it reduces significantly the predicted amount of shock heating. We can calculate the variation of the kinetic energy of a particle located at some distance  $r$  from the center of the satellite,  $\Delta E$ , due to impulsive heating at each pericentric passage in the extended mass distribution of a primary isothermal halo (see also Mayer et al. 2002; Taffoni et al. 2003). Gnedin, Hernquist, & Ostriker (1999) have shown that for orbits as eccentric as those considered here, we can approximate the trajectory of the satellite with a straight line path and write

$$\langle \Delta E \rangle = \frac{1}{2} \left( \frac{GM_0}{R_{\text{per}}^2 V_{\text{per}}} \right)^2 \frac{r^2 \pi^2}{3} \left( \frac{R_{\text{per}}}{R_{\text{max}}} \right)^2 (1 + \omega\tau)^{-2.5}, \quad (6)$$

where  $M_0$  and  $R_{\text{max}}$  are the total mass and radius, respectively, of the primary halo, which are assumed equal to the mass and radius within the apocenter of the satellite’s orbit, and  $V_{\text{per}}$  is the satellite’s velocity at the pericenter of the orbit. These parameters are equal to  $M_0 = 8.4 \times 10^{11} h^{-1} M_{\odot}$ ,  $R_{\text{max}} = 105 h^{-1}$  kpc, and  $V_{\text{per}} = 345 \text{ km s}^{-1}$ . The last term in the product is the first-order adiabatic correction with  $\omega$  and  $\tau$  being the orbital frequency for a particle at radius  $r$  and the duration of the tidal shock, respectively.

For a particle at a distance of  $r = 0.7 h^{-1}$  kpc from the center of the satellite,  $\Delta E$  without the adiabatic correction is roughly equal to 20% of its binding energy,  $E_{\text{bind}}$ , after three tidal shocks. Instead,  $\Delta E/E_{\text{bind}}$  is already greater than 1 at a radius of  $r = 1.75 h^{-1}$  kpc, despite the fact that the tidal radius of the satellite is much larger. However, once the adiabatic correction is included, the ratio  $\Delta E/E_{\text{bind}}$  is reduced by nearly 90%, explaining why the satellite is barely affected by the tidal shocks in its inner regions. Note that in order to incorporate the effect of the adiabatic correction in the simulations, one needs to model

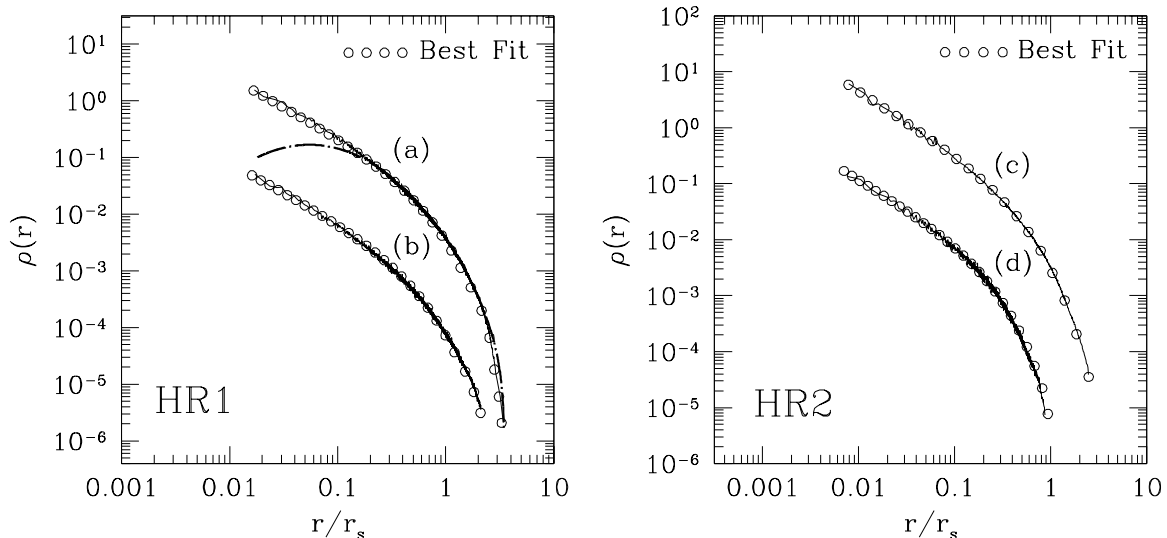


FIG. 3.— Density profiles of substructure halos from our individual satellite simulations (*solid curves*), together with fits to the density structure obtained using eq. (5) (*circles*). The profiles are shown for models HR1 (*left*) and HR2 (*right*) and for two different timescales in the orbital evolution. In both panels, the density profiles corresponding to the lower curves are vertically shifted downward by 1.5 dex for clarity. Curves (a) and (b) correspond to  $t = 1.69 T_{\text{orb}}$  and  $t = 2.71 T_{\text{orb}}$ , respectively. These curves are best described by fitting parameters  $(\gamma, r_b/r_s) = (1.02, 2.69)$  and  $(\gamma, r_b/r_s) = (1.00, 2.06)$ , respectively. Curves (c) and (d) correspond to  $t = 1.33 T_{\text{orb}}$  and  $t = 2.36 T_{\text{orb}}$  and the best fit parameters are  $(\gamma, r_b/r_s) = (1.02, 0.43)$  and  $(\gamma, r_b/r_s) = (0.99, 0.19)$ , respectively. The fits are satisfactory over 4 orders of magnitude in density and 2 orders of magnitude in radius and for satellites having concentration parameters that differ by more than a factor of 2. The thick dotted line shows the density profile corresponding to the parabolic circular velocity fitting formula proposed by S02 with  $a = 0.45$ , the median value of their best fits to substructure halos (see text for details).

the inner regions of the subhalo quite accurately. This means resolving down to sub-kiloparsec scales in the first place and also avoiding non-equilibrium initial conditions or coarse mass resolution. The latter could affect the orbital frequencies of the dark matter particles, which might well end up in a region of phase space that is not protected by the adiabatic invariance anymore (this problem is reminiscent of the difficulty that  $N$ -body simulations of low resolution have in resolving resonances in stellar systems; see Weinberg & Katz (2002)).

Figure 3 shows the density profiles for two different timescales in the orbital evolution of models HR1 and HR2 (solid curves). Fits to the density structure of the substructure halos using equation (5) and obtained by  $\chi^2$  minimization are also shown, as circles. Model HR1 (*left*) is plotted at  $t = 1.69 T_{\text{orb}}$  and  $2.71 T_{\text{orb}}$ , which correspond to  $\sim 0.4$  Gyr after the satellite has concluded its second and third pericentric passages, respectively. Model HR2 (*right*) is plotted at  $t = 1.33 T_{\text{orb}}$  and  $2.36 T_{\text{orb}}$ , which correspond to  $\sim 0.4$  Gyr before the conclusion of the satellite’s second and third pericentric passages, respectively. Note that for clarity we offset the lower curves in both panels by 1.5 dex. Clearly, the structure of our stripped satellites is reasonably well reproduced by the proposed fitting formula. We should note that this formula works well in the case of the lower concentration satellite for the entire orbital evolution. On the other hand, the case of the  $c_{\text{sat}} = 21$  satellite is somehow slightly different. The fitting function works better for the last stages of the orbital evolution, at which the satellite has suffered significant mass loss. This is just reflecting the resilience to tidal stripping of the high concentration satellite during the early stages of the evolution and the fact that the mass loss is more gradual compared to the low concentration model, even from the outer regions. Finally, for comparison we show

the density profile resulting from the fitting formula proposed by S02 (*thick dotted line*) to describe the structure of their subhalos (see their eq. [1]), plotted down to the limit of our force resolution. The values for  $r_{\text{max}}$  and  $V_{\text{max}}$  in their formula are taken directly from the particular subhalo. In addition, we adopt a value for the parameter  $a$  in their equation that is equal to the median of their best fits,  $a = 0.45$ . Compared to the density profiles describing the structure of our satellites, the latter profile has a substantially shallower slope on scales comparable to the sizes of the dSphs. Interestingly, the density reaches even negative values at a finite radius, demonstrating that its use should be avoided.

## 2.2. Substructure in Hierarchical Cosmological Simulations

In this section, we present results from a set of high resolution  $\Lambda$ CDM cluster simulations (Diemand et al. 2004b). The initial conditions are generated with the GRAFIC2 package (Bertschinger 2001). We begin with a  $300^3$  particle cubic grid with a comoving cube size of 300 Mpc (particle mass  $m_p = 2.6 \times 10^{10} h^{-1} M_\odot$ ). At  $z = 0$  we identify several clusters for resimulating at higher resolution, using refinement factors of 6, 9, and 12 in length (216, 729, and 1728 in mass), so that the mass resolution is  $m_p = 1.5 \times 10^7 h^{-1} M_\odot$  in the highest resolution run. We label these three runs as R6, R9 and R12, after their refinement factors. At  $z = 0$  the refined cluster contains  $1.8 \times 10^6$  particles within the virial radius in run R6,  $6 \times 10^6$  in R9, and  $1.4 \times 10^7$  in R12. Note that we define the virial radius of the clusters,  $R_{\text{vir}}$ , to be the distance from the center at which the mean enclosed density is  $178 \Omega_m^{0.45} \approx 103.5$  times the critical value  $\rho_{\text{crit}}$  (Eke, Cole, & Frenk 1996). The softening length is comoving from the start of the simulation ( $z \simeq 40$ ) to  $z = 9$ . From  $z = 9$  until



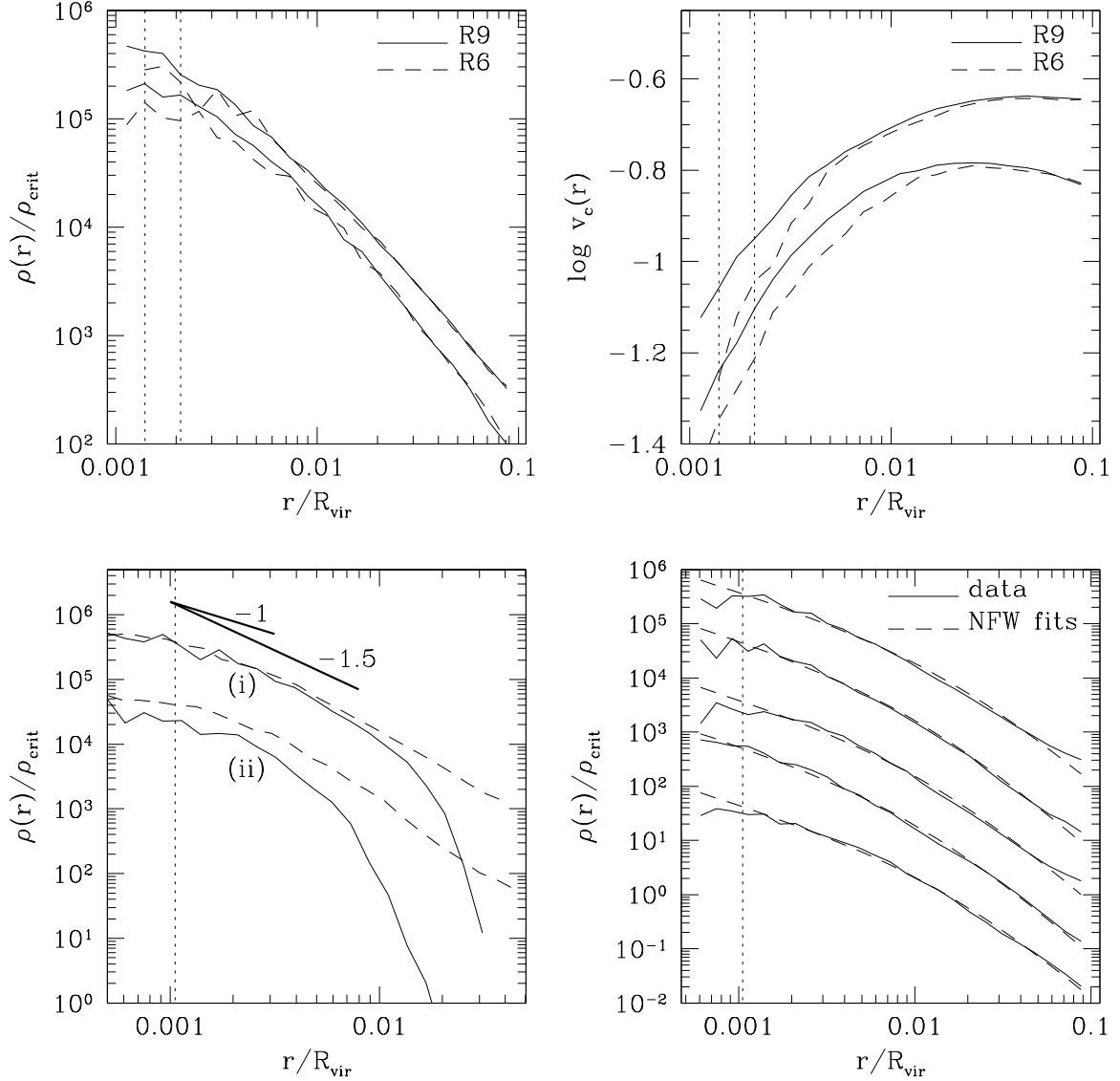


FIG. 4.— *Top*: Density (*left*) and circular velocity (*right*) profiles of two subhalos simulated at two different resolutions. Circular velocities are expressed in units of the maximum circular velocity of the parent halo. In simulation R9 (solid lines), the subhalos contain  $3.4 \times 10^4$  and  $1.4 \times 10^4$  particles, while in R6 (dashed lines) they contain a factor of 3.375 fewer particles. The convergence in the circular velocity profiles between the two resolutions is significantly slower on account of the cumulative nature of this quantity. This demonstrates that it is erroneous to use the circular velocity to compute the structural properties of substructure. *Bottom left*: Density profiles of two heavily stripped substructure halos in simulation R12 before entering the primary halo (*dashed lines*) and at present (*solid lines*). Subhalo (i) is shown at  $z = 0.80$  and just before the second pericentric passage. Subhalo (ii) is shown at  $z = 0.94$  and just before the fourth pericentric passage and is offset by 1 dex to avoid overlap. The numbers near the thick solid lines indicate the power slope of those lines. Both subhalos have of the order of  $N = 2 \times 10^4$  particles before entering the host. The cosmological subhalos maintain their steep inner density slope even after several pericentric passages. *Bottom right*: Density profiles of the five most massive halos in simulation R12 (solid lines). The best-fit NFW profiles are also plotted (*dashed lines*). To avoid overlap the lower four density profiles are vertically shifted by 1, 2, 3, and 4 dex from the top to the bottom. These five halos are resolved with more than  $2 \times 10^5$  particles. In all panels the vertical dotted lines show the adopted force resolution.

the present we use a physical softening length of 2.1, 1.4, and  $1.05 \times 10^{-3} R_{\text{vir}}$  for R6, R9, and R12 respectively.

In the top panels of Figure 4, we show the density (*left*) and circular velocity (*right*) profiles of two distinct substructure halos simulated at two different resolutions. In simulation R9 (*solid lines*), the two subhalos contain  $N = 3.4 \times 10^4$  and  $N = 1.4 \times 10^4$  particles, respectively, whereas in simulation R6 (*dashed lines*) the same subhalos contain a factor of 3.375 fewer particles. The vertical dotted lines show the adopted force resolution. Densities are expressed in units of the present critical density for closure,  $\rho_{\text{crit}} = 3H_0^2/8\pi G$ , and the virial radius of the parent halo is equal to  $R_{\text{vir}} = 1.225h^{-1}$  Mpc. The profiles of the cosmological satellites are to be trusted only up to the resolution limit set by two body relaxation (Diemand et al. 2004a). We note that the convergence of the circular velocity profiles is much weaker than that of the density profiles at different resolutions, in agreement with the results presented in § 2.1. As the circular velocity is a cumulative quantity, numerical effects show up at comparatively larger radii, where the density profiles have already converged, biasing the circular velocity profiles. Therefore, one should be especially cautious when using the circular velocity profiles obtained at one particular resolution to provide fitting functions to systems whose typical scales fall below such resolution, as done in S02.

In the bottom panels of Figure 4, we present results regarding substructure halos taken from our highest resolution simulation (R12). The density profiles of two heavily stripped subhalos before entering the primary halo (*dashed lines*) and at present (*solid lines*) are shown in the bottom left panel. These satellites have of the order of  $N = 2 \times 10^4$  particles before entering the host. The subhalo denoted “(i)” is shown at  $z_{\text{in}} = 0.80$  and at present just before the second pericentric passage ( $r_{\text{min}} = 0.21R_{\text{vir}}$ ). The second subhalo, denoted “(ii),” is offset by 1 dex to avoid overlap and is shown at  $z_{\text{in}} = 0.94$  and at present just before the *fourth* pericentric passage ( $r_{\text{min}} = 0.15R_{\text{vir}}$ ). The thick solid lines indicate two critical values for the inner slope,  $\rho(r) \propto r^{-1}$  and  $\rho(r) \propto r^{-1.5}$ . This plot illustrates that the substructures maintain the steep inner density slope that they had before entering the primary halo, even after several pericentric passages. These heavily stripped satellites have outer profiles consistent with an exponential cutoff. Even though these cosmological simulations are state-of-the-art by the current standards, the resolution in these stripped satellites is still too low for us to draw robust conclusions regarding the evolution of their inner structure.

Finally, the bottom right panel of Figure 4 shows the density profiles of the five most massive substructure halos in this simulation (*solid lines*) together with the best fit NFW profiles (*dashed lines*). To avoid overlap, the lower four density profiles are each vertically shifted by 1 dex from each other. These five halos are resolved with more than  $N = 2 \times 10^5$  particles, and their density profiles are described reasonably well by the NFW profile. These halos entered the host system quite late and have typically made only one orbit; however, these most massive halos represent the ones that would be associated with the dSphs, according to S02. We can plausibly trust their central structure to  $0.002R_{\text{vir}}$ , which corresponds to about 500 pc when scaled to the Galaxy. At this radius the density pro-

files are still cuspy, with central slopes between  $-1$  and  $-1.5$ .

We end by emphasizing that the behavior of the satellites in the time-dependent cosmological tidal field is not obviously similar to that our individual subhalos exhibit when evolved in a static host potential. The latter are spherical systems with isotropic velocity dispersion tensors, whereas the cosmological satellites presented here are in general triaxial, anisotropic systems, and they suffer additional artificial heating from background particles and physical heating from encounters with other substructures. It is remarkable, therefore, that our findings regarding the way that tidal interactions affect the central density cusps converge in these two radically different regimes: the inner density profiles remain cuspy to the resolution limit of the simulations.

### 3. DWARF SPHEROIDAL KINEMATICS IN CDM SUBHALOS

Cosmological numerical simulations confirm that isolated halos in the mass range  $10^7 - 10^{10} M_{\odot}$  have central cusps not shallower than  $\rho(r) \propto r^{-1}$ , on scales comparable to the ones probed by the stars in the dSph satellites (Moore et al. 2001; Colin et al. 2003). Our results in § 2 indicate that an initial cuspy satellite will retain its cusp in the presence of a tidal field. Therefore, it is an interesting exercise to attempt to reproduce the observed kinematics of the dSphs assuming cuspy dark matter distributions, and to constrain the maximum mass or circular velocity of their host halos. The advantage of our approach lies in the fact that we have sufficient numerical resolution, and therefore there is no need of extrapolating the inner density slopes to scales smaller than the force resolution, as done by S02.

The dynamics of a spherically symmetric stellar distribution embedded in a spherical dark matter potential can be described by the lowest order Jeans equation, assuming that the two components are in equilibrium and that there are no net streaming motions (e.g., rotation):

$$\frac{d}{dr}(\rho\sigma_r^2) + \frac{2\beta}{r}\rho\sigma_r^2 + \rho\frac{d\Phi}{dr} = 0 \quad (7)$$

(Binney & Tremaine 1987), where  $\rho(r)$  and  $\sigma_r(r)$  are the density profile and the radial velocity dispersion of the tracer stellar population, respectively,  $\Phi(r)$  is the underlying dark matter gravitational potential, and  $\beta$  describes the velocity anisotropy of the stars. The solution of the Jeans equation (7) with the boundary condition  $\rho(r) \rightarrow 0$  at  $r \rightarrow r_t$  for  $\beta = \text{const}$  reads

$$\rho\sigma_r^2 = r^{-2\beta} \int_r^{r_t} r^{2\beta} \rho \frac{d\Phi}{dr} dr, \quad (8)$$

where  $r_t$  is the tidal radius of the stellar component.

However, the quantity that can be measured and compared with observations is the line-of-sight velocity dispersion,  $\sigma_p$ , at projected distance  $R$  from the center of the dwarf, which is given by

$$\sigma_p^2(R) = \frac{2}{I(R)} \int_R^{r_t} \left(1 - \beta \frac{R^2}{r^2}\right) \frac{\rho\sigma_r^2(r, \beta)r}{\sqrt{r^2 - R^2}} dr \quad (9)$$

(Binney & Mamon 1982; Binney & Tremaine 1987), where  $I(R)$  is the surface distribution of the tracer population:

$$I(R) = 2 \int_R^{r_t} \frac{r\rho(r)}{\sqrt{r^2 - R^2}} dr. \quad (10)$$

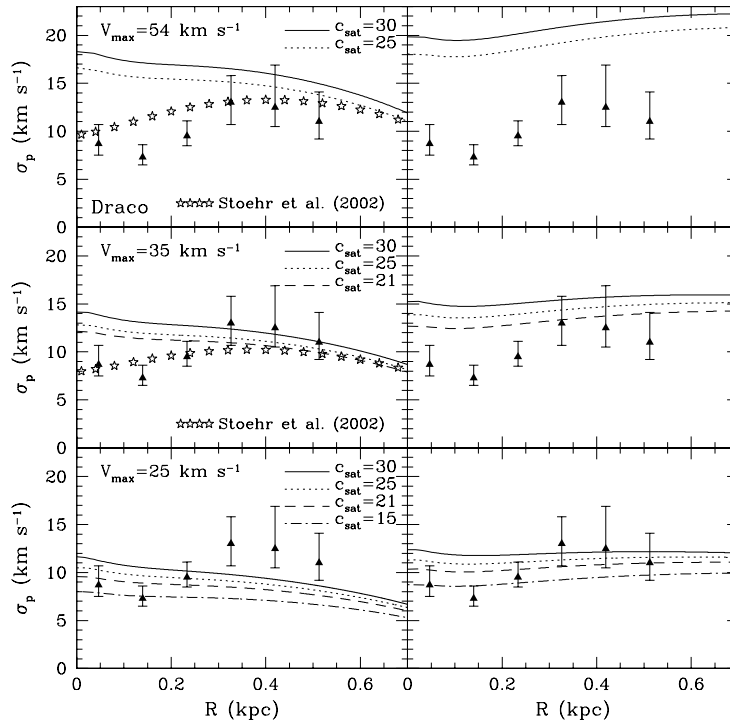


FIG. 5.— Observed line-of-sight velocity dispersions for the dSph Draco (*triangles*), compared with those predicted for stellar systems embedded in dark matter halos with structure similar to the ones of our simulated subhalos. Each pair of panels refers to a single value of  $V_{\max}$ , while the various lines correspond to different values of  $R_{\max}$  in the same range as in S02 (see text for details). The three plots on the left show results assuming a tidal radius for Draco equal to the *optical radius* measured by Odenkirchen et al. (2001) and also adopted by S02. The panels on the right show results for the same range of parameters, but for tidal radii 3 times as large. The filled points correspond to the results obtained assuming the parabolic fits to the circular velocity profiles adopted by S02. From top to bottom, the results for  $V_{\max} = 54$ , 35, and 25  $\text{km s}^{-1}$  are shown. Globally, the observed velocity dispersion profile is better reproduced by subhalos with  $V_{\max} = 25 \text{ km s}^{-1}$  and assuming a significantly larger than the nominal tidal radius.

We solve equation (9) using the customary King profile for the stellar population of the dSph galaxies,

$$\rho_*(r) \propto \frac{1}{z^2} \left[ \frac{1}{z} \cos^{-1}(z) - (1 - z^2)^{1/2} \right] \quad (11)$$

(King 1962), where  $z \equiv [1 + (r/r_c)^2]/[1 + (r_t/r_c)^2]$  and  $r_c$  denotes the core radius of the profile. For Fornax and Draco, we use the parameters from Mateo (1998) and Odenkirchen et al. (2001), respectively, similarly as in S02. Note that the normalization in equation (11) is not important for the purpose of our analysis, since it cancels out. Motivated by the structure of our simulated subhalos from the cosmological simulations, we assume that the dark matter halos associated with the dwarf galaxies follow the NFW density profile. This provides a lower limit to the recovered velocity dispersions, since there is evidence in favor of steeper central density cusps on these scales (e.g., Moore et al. 2001). Our results are not sensitive to the presence of the exponential cutoff, since the fitting formula of equation (5) differs appreciably from the NFW density profile only near the break radius  $r_b$ . This is larger than the tidal radii of the stellar components of the dSphs, where the integral in equation (9) has to be truncated anyway. In addition, we checked that any eventual differences in the resulting projected stellar velocity dispersions were negligible even when we considered models with stellar tidal radii significantly larger than the nominal values (see below).

We consider halos having both a maximum circular velocity,  $V_{\max}$ , and a corresponding radius,  $R_{\max} = R(V_{\max})$ ,

within the range considered by S02. In practice, for each value of  $V_{\max}$  there is only a limited range of halo concentrations such that  $R_{\max}$  is consistent with the values measured by S02 for their subhalos. In Figures 5 and 6, we show the results of the comparison for Draco and Fornax, respectively, assuming isotropic stellar orbits. The observed velocity dispersion profiles are reproduced from Mateo (1998) for Fornax and from Kleyna et al. (2002) for Draco. In some of these panels, where the relative information is available, we overplot the results obtained adopting the parabolic fitting function of the form proposed by S02 for their subhalos (*filled points*). We remind the reader that the density profiles corresponding to this parabolic function have substantially shallower inner slopes at scales comparable to the sizes of the dSphs than the profiles describing the density structure of our satellites. Each pair of panels refers to a single value of  $V_{\max}$ . The three panels on the left show results assuming a tidal radius equal to that adopted by S02, while the panels on the right assume tidal radii 3 times as large.

It is immediately apparent that subhalos with  $V_{\max} \sim 50 \text{ km s}^{-1}$  would yield velocity dispersions significantly above the observed values for both Fornax and Draco, once the cuspy density profiles consistent with the structure of our satellites were used. The discrepancy becomes even worse if we allow the stellar component to have a tidal radius larger than the nominal value estimated by fitting the star counts to a King profile. Recent observational studies of Draco show no evidence of tidal tails, lending support to the view

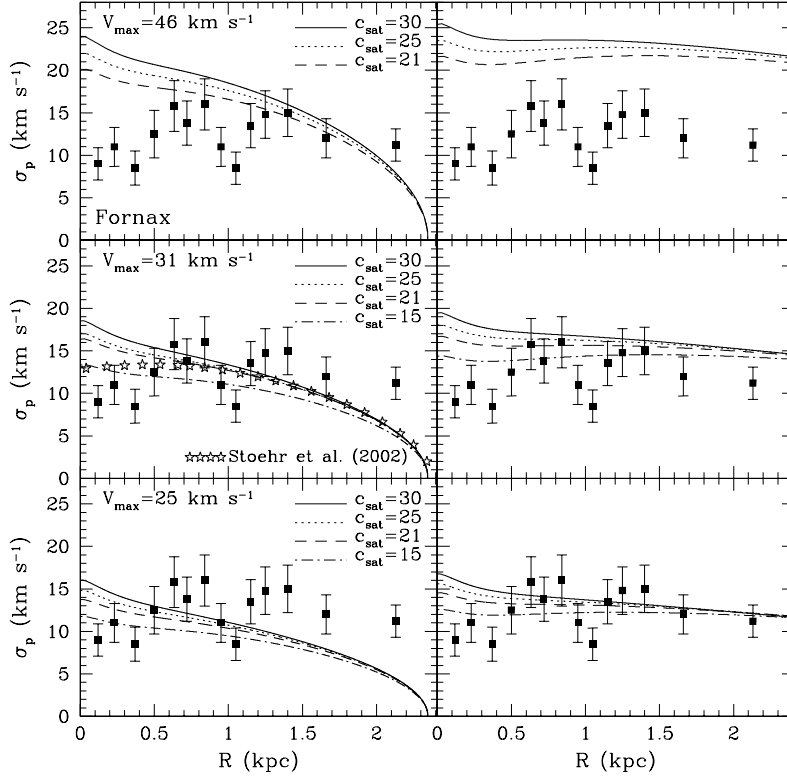


FIG. 6.— Same as Figure 5, but for the dSph Fornax (*squares*). The three plots on the left show results assuming a value for the tidal radius taken from the review of Mateo (1998). From top to bottom, the results for  $V_{\max} = 46, 31,$  and  $25 \text{ km s}^{-1}$  are shown. Similarly to the case of Draco, the stellar velocity dispersion is better reproduced by subhalos with  $V_{\max} = 25 \text{ km s}^{-1}$  and assuming a tidal radius 3 times larger than the nominal value (*right*).

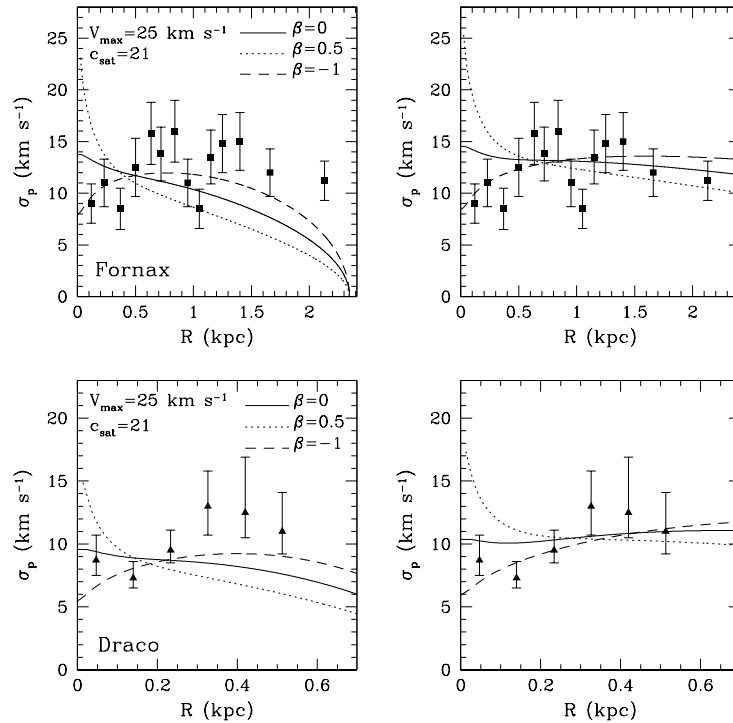


FIG. 7.— Kinematics of Fornax (*top*) and Draco (*bottom*), compared with those expected for stellar systems embedded within NFW subhalos with  $V_{\max} = 25 \text{ km s}^{-1}$ . Different values for the anisotropy parameter  $\beta$  in the velocity distribution of the stellar component have been considered. The solid lines correspond to isotropic models, whereas the dotted and dashed lines to radially and tangentially anisotropic models, respectively. The plots on the left show results for values of the tidal radii of the stellar component equivalent to those used by S02, while the plots on the right correspond to tidal radii 3 times as large. Models with mildly tangentially anisotropic distribution of stellar orbits better reproduce the observed velocity dispersion profiles of both Draco and Fornax. Radially anisotropic models overestimate the central stellar velocity dispersion and make the curves decrease more steeply with distance, contrary to the trend in the observational data.

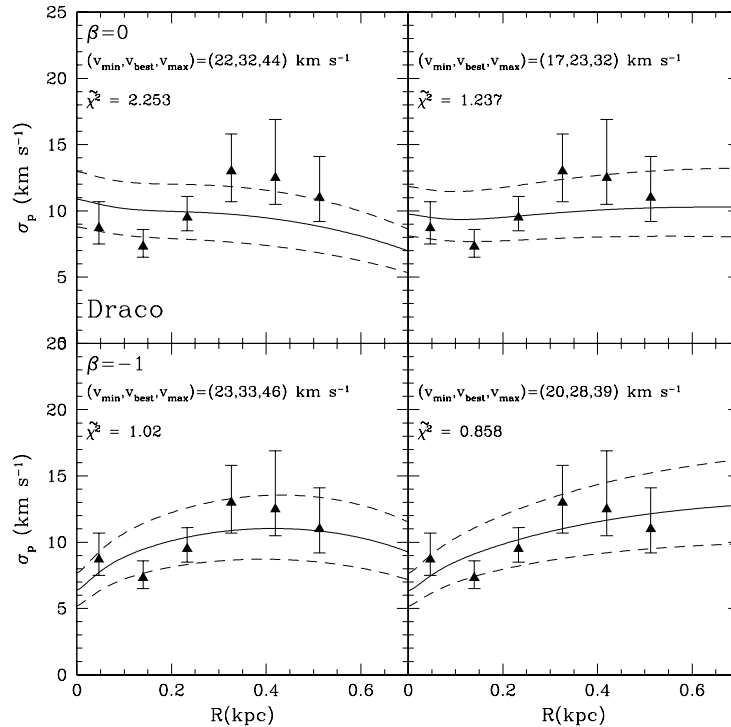


FIG. 8.— Best fit models (*solid lines*) and  $3\sigma$  intervals (*dashed lines*) for the kinematics of Draco, assuming isotropic (*top*) and tangentially anisotropic (*bottom*) models for the stellar distribution. The stars are embedded in the potential wells of our stripped satellites and follow a King profile. The panels on the left show results adopting a tidal radius equal to the nominal value, whereas the panels on the right show results for tidal radii 3 times as large (see text for details). Keeping the concentration parameter fixed ( $c = 21$ ), we fit by  $\chi^2$  minimization the maximum circular velocity  $V_{\max}$ . The best fit value of  $V_{\max}$  corresponds to  $v_{\text{best}}$ , whereas  $v_{\text{min}}$  and  $v_{\text{max}}$  bracket the  $3\sigma$  intervals. The quality of the fits in terms of the reduced  $\chi^2$  is also indicated for the different cases. Subhalos with  $V_{\max}$  in the range  $20 - 35 \text{ km s}^{-1}$  provide the best fit to the data, while  $V_{\max} > 40 \text{ km s}^{-1}$  are  $3\sigma$  or more away from the best fit.

that the optical radius is only a lower limit to the true physical boundary of the system (Odenkirchen et al. 2001; Kleyna et al. 2002; Piatek et al. 2002; Klessen, Grebel, & Harbeck 2003), and this might also be true for the majority of the dSphs. By considering subhalos with  $V_{\max} \sim 30 \text{ km s}^{-1}$ , we match satisfactorily only the velocity dispersion data points at the outermost radii, which have the largest error bars. Subhalos with  $V_{\max} = 25 \text{ km s}^{-1}$  reproduce the observed stellar velocity dispersions reasonably well for the entire range of parameters considered. This conclusion is in disagreement with that reached by S02, simply because of their use of a parabolic fitting function, and suggests that there is no room for entirely solving the substructure problem by simply changing the way the velocities are mapped. Globally, the observed velocity dispersion profile is better reproduced by assuming a larger tidal radius, even though the predicted profiles always tend to be slightly flatter than the data.

The situation can be improved significantly by adopting a weakly tangentially anisotropic velocity distribution for the stars, as shown in Figure 7. Indeed, for  $\beta = -1$  (*dashed lines*), subhalos with  $V_{\max} = 25 \text{ km s}^{-1}$  are nicely consistent with most of the data points for both Draco and Fornax. Note that a mildly tangentially anisotropic distribution of stellar orbits was required by Kleyna et al. (2002) in their best fit models to the kinematics of Draco. Moreover, Lokas (2002) finds that the steeper the dark halo inner density cusp, the more tangential a stellar velocity distribution is required to fit the data for both Draco and Fornax. Interestingly, modeling based on high-resolution Keck spec-

troscopy of six Virgo dwarf elliptical galaxies having an average line-of-sight velocity dispersion in the range  $\sigma \sim 25 - 50 \text{ km s}^{-1}$  also yields for most of them best fit models to their kinematics that are consistent with mildly tangentially anisotropic orbits (Geha, Guhathakurta, & van der Marel 2002). Radially anisotropic models with  $\beta = 0.5$  (*dotted lines*) overestimate the central stellar velocity dispersion by a factor of  $\sim 2$  and lead to steeply declining velocity dispersion profiles, contrary to the trend in the observational data. As in the case of the isotropic orbits, if we assume a tidal radius 3 times larger (*right*) the match to the stellar velocity profiles becomes better.

In Figures 8 and 9, we present the best fit models (*solid lines*), together with the  $3\sigma$  intervals (*dashed lines*) for Draco and Fornax respectively, assuming isotropic (*top*) and tangentially anisotropic (*bottom*) models. In each case, we fix the value of the concentration parameter and fit, by  $\chi^2$  minimization the maximum circular velocity  $V_{\max}$  with the two different values for the tidal radius of the stellar component. Note that for Draco the best fit is calculated taking into account that the error bars are asymmetric. The fixed concentration parameter we used ( $c = 21$ ) is consistent with nearly all the profiles of the subhalos in S02. Higher concentration models would imply lower values of  $V_{\max}$ , and therefore our choice is conservative. This more detailed analysis shows that subhalos with  $V_{\max}$  in the range  $20 - 35 \text{ km s}^{-1}$  provide the best fit to the data and also that the high values favoured by S02,  $V_{\max} > 40 \text{ km s}^{-1}$ , are  $3\sigma$  or more away from the best fit. Determining the absolute best fit to the data requires fit-

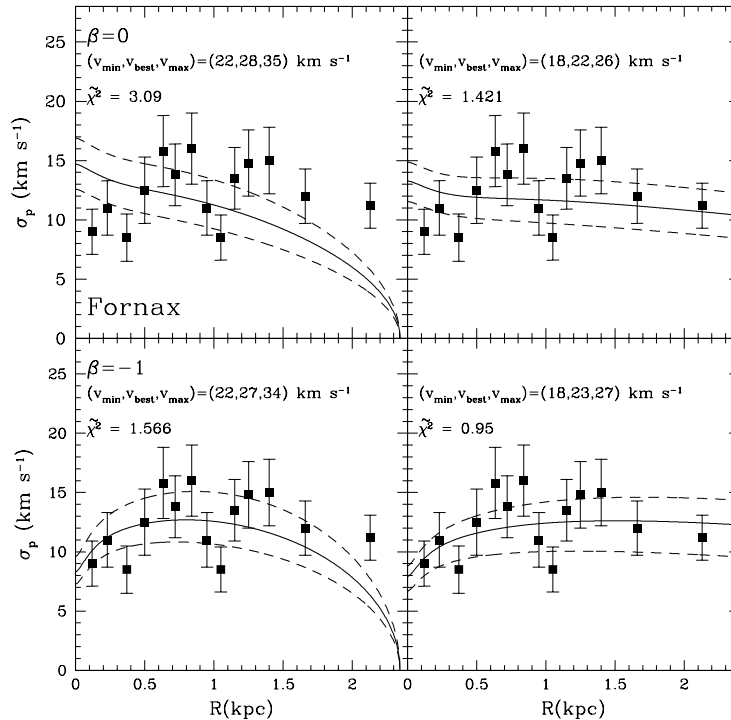


FIG. 9.— Same as Figure 8, but for the dSph Fornax. Similarly to the case of Draco, subhalos with  $V_{\max}$  in the range  $20 - 30 \text{ km s}^{-1}$  provide the best fit to the data (solid lines), while  $V_{\max} > 35 \text{ km s}^{-1}$  are  $3\sigma$  (dashed lines) or more away from the best fit.

ting more parameters, which is clearly outside the scope of the present paper (however, see Lokas 2002). In general, the degree of anisotropy can be a function of radius instead of being simply a constant parameter. In models in which the dSphs are formed by the tidal stirring and transformation of disk-like systems similar to present-day dwarf irregular galaxies (Mayer et al. 2001a,b), the remnant is a triaxial system whose velocity anisotropy depends on the radius. The remnants produced in those simulations can be fitted by either an exponential or a King profile, similar to the observed dSphs. Although there is considerable scatter in their structural properties (Mayer et al. 2001b), in general the stellar orbits are tangentially anisotropic in the central regions (at distances equivalent to the core radii of Draco and Fornax) and become nearly isotropic or slightly radially anisotropic in the outer regions, where they are partially flattened by rotation. The interesting point is that values of  $\beta$  ranging from  $-0.5$  to  $-1.3$  are typical in the region where most of their bound mass is. This result is confirmed by recent gas-dynamical simulations with radiative cooling and heating and star formation (L. Mayer et al. 2004, in preparation; Mayer & Wadsley 2003) and lends support to the results shown in Figure 7 for  $\beta = -1$ . Note that Zentner & Bullock (2003) suggested that a mild radial anisotropy for the dSphs equal to  $\beta = 0.15$  should be expected because the latter value is typical of the central regions of simulated CDM halos, where the dwarfs actually reside. However, our results highlight that this is not necessarily the case. The tidally stirred stellar components develop a tangential anisotropy even though they evolve inside an initially isotropic dark matter halo because their evolution is governed by non-axisymmetric, bar/buckling instabilities (Mayer et al. 2001b).

We end by emphasizing that if the density profiles of the

subhalos models are initially steeper than an NFW profile by either having intrinsically steeper inner slopes (as might be possible for some of the satellites in our cosmological runs; see § 2.2) or becoming steeper as a result of the adiabatic contraction following the collapse of baryons (Blumenthal et al. 1986), circular velocities even lower than the above values would be required to acceptably reproduce the observed data.

#### 4. DISCUSSION

The results presented in the previous sections indicate that the conversion between  $\sigma_*$  and  $V_{\max}$  initially adopted by Moore et al. (1999) and Klypin et al. (1999) is reasonable. Low values of  $V_{\max}$  are required if the dSphs are embedded in CDM halos. There is a second, phenomenological reason why the observed satellites should not reside in halos as massive as the ones postulated by S02. In this case, their baryonic components would lie within a very small region corresponding to only 1% of the virial radius of the object, posing a problem for structure formation scenarios. Indeed, in the prevailing galaxy formation paradigm (e.g., Fall & Efstathiou 1980; Mo, Mao, & White 1998), the baryons condense into a rotationally supported structure whose size is determined by the initial spin parameter  $\lambda$  and concentration  $c$  of the dark matter halo, and the fraction of mass and angular momentum of baryons relative to that of the halo. Assuming that the specific angular momentum of baryons is conserved during their infall and that the halo and baryons start with the same specific angular momentum (Mo, Mao, & White 1998), one can easily show that for a halo as massive as  $V_{\text{vir}} = 50 \text{ km s}^{-1}$ , a spin parameter equal to  $\lambda < 0.01$  would have been needed for the baryons to collapse to the observed size of Draco. However, such a small value for

the spin occurs in less than 1% of the cosmological halos (Warren et al. 1992; Lemson & Kauffmann 1999; Gardner 2001).

The distribution of spin parameters has been measured so far only for isolated halos and at mass scales larger than those of dwarf galaxies (e.g., Bullock et al. 2001b; Gardner 2001). Although a new systematic analysis overcoming the above limitations will be needed in the future, we made the first step forward in this direction and we measured the spin parameter  $\lambda$  for some of our subhalos. In particular, we selected ten isolated halos from the high resolution region of run R6 and six subhalos within the virial radius of the cluster in both runs R6 and R12. All halos are selected by mass ( $M_{\text{vir}} \simeq 6.3 \times 10^{10} h^{-1} M_{\odot}$ ). The spin parameters are measured at a radius equal to  $0.5 r_{\text{vir}}$  for the isolated halos, where  $r_{\text{vir}}$  denotes the halo virial radius, and at  $0.7 r_t$  for the subhalos, where  $r_t$  denotes the subhalo tidal radius. The  $\lambda$ -values we found for both isolated halos and subhalos are between 0.024 and 0.12 and follow a log-normal distribution with  $\bar{\lambda} = 0.039$  and  $\sigma_{\lambda} = 0.55$  in agreement with previous studies using a much larger halo sample (e.g., Bullock et al. 2001b). This finding confirms our phenomenological argument that the dSph satellites could not be embedded in very massive halos. Finally, it is interesting to note that the comparison of the spin parameters of the same subhalos in runs R6 and R12 shows that they are independent of resolution. Removal of baryons from an initially more extended system by tidal stripping, by supernova feedback, or even by photoevaporation from the UV background cannot be invoked to reduce the size of the baryonic component of the dwarfs at a later stage, because the halo would have been massive enough to suppress all these mechanisms (Benson et al. 2002b). One then would have to rely on some catastrophic loss of angular momentum during baryonic collapse, but there is no obvious reason why this should have happened.

Recently, Kravtsov, Gnedin, & Klypin (2004) proposed a qualitatively different solution to the missing satellites problem. Using high resolution cosmological simulations of the formation of a Milky Way sized halo in a  $\Lambda$ CDM universe, these authors argued that the luminous dSphs in the Local Group can be identified with halos that had considerably higher masses and circular velocities when they formed at high redshift. Their model provide a convincing explanation as to why the dSphs could retain their gas and form stars after reionization and indicates that they are embedded in dark matter halos that suffered dramatic mass loss due to tidal stripping. We believe that the major difference between the subhalos' density structure found in our study and that claimed by S02 is due to resolution effects affecting the determination of the circular velocity. On the other hand, the reduced concentration that H03 find for their simulated satellites may be an artifact of non-equilibrium initial conditions combined with numerical resolution, rather than reflecting the influence of tidal shocks on the inner regions of the satellites. The evolution of the internal structure is expected to be dramatically different for models that are not self-consistent compared to models for which one considers carefully the exact dynamics. Regarding this issue, Kazantzidis et al. (2004) found that NFW satellites initialized using the Maxwellian ap-

proximation experience artificially accelerated mass loss and can completely disrupt in an external tidal field. The same satellites, however, survive in identical experiments once the exact self-consistent velocity distribution of the model is taken into account.

Of course, one cannot exclude that some dynamical mechanism other than tidal interactions might have been responsible for lowering the concentration of the subhalos. For example, if bars are effective in redistributing the angular momentum between the baryons and the halo (Weinberg & Katz 2002), then the dSphs could have been strongly affected by this mechanism if they originate from the morphological evolution of tidally stirred dwarf irregular galaxies. Indeed, tidal stirring always incorporates a strong bar instability phase. However, recent work suggests that the amount of angular momentum that a bar transfers to the halo is not enough to turn the inner cusp into a core (Sellwood 2003).

The results presented in this paper argue that there is no simple solution to the substructure problem within CDM models. The kinematics of the dSphs are indeed a reasonable tracer of their dark halo potential wells. However, their kinematics can also be accurately reproduced with dark halo density profiles that are nearly flat in the center (see Figures 5 and 6). The latter fact illustrates the need to use better quality data and perhaps higher order moments of the velocity distribution to break this degeneracy and constrain the central cusp slopes (Lokas 2002). Our findings also have important implications for indirect dark matter detection experiments attempting to observe the resulting  $\gamma$ -ray flux from neutralino annihilation. The expected flux depends sensitively on the line-of-sight integral of the square of the mass density. This integral changes by more than one order of magnitude between the NFW and the much shallower density profiles found by S02, as pointed out by the same authors in a more recent paper (Stoehr et al. 2003). With such shallow density profiles, Air-Shower-Cerenkov telescopes like VERITAS and MAGIC might barely detect the emission from the Galactic center and would completely miss that coming from the dSphs. However, for dark matter particle candidates with properties consistent with some of the minimal supersymmetric models (Bergström et al. 1998) and with the persistently steep inner density profiles found in this paper, the Galactic center would be easily detected and the dSph satellites still represent potentially valuable targets (Calcáneo-Roldán & Moore 2000).

## 5. SUMMARY

We have investigated the structural evolution of substructure, using a set of high-resolution cosmological  $N$ -body simulations, coupled with simulations of the tidal stripping of individual satellites orbiting within a static host potential and employing up to  $N = 10^7$  particles. Our main results and conclusions may be summarized as follows:

1. Cuspy satellite halos on eccentric orbits do not experience significant mass redistribution in their centers, and they retain the same steep inner density slope even after several strong pericentric tidal shocks. This result is valid for our high-resolution cosmological simulations, in which the satellites evolve within

a time-dependent cosmological tidal field, and for our simulations of individual subhalos orbiting within a massive host system modeled as a fixed potential.

2. Convergence in the circular velocity profiles occurs much more slowly than that of the density profiles. This is due to the fact that low central resolution propagates to larger radii on account of the cumulative nature of the former quantity. This discourages any attempt to use circular velocities of simulated satellites to derive their structural properties.
3. The density structure of tidally stripped cuspy halos can be well approximated by a simple fitting function (eq. [5]), comprising an unmodified power-law central slope and an exponential cutoff, that describes the satellite's boundary imposed by the tides.
4. The predicted kinematics of the dSph galaxies Fornax and Draco, assuming that they are embedded in the potential wells of our tidally stripped satellites, were compared to the observed stellar velocity dispersion profiles. Adopting isotropic and tangentially anisotropic models for the stellar component, we find that dark matter halos with maximum circular velocities in the range  $V_{\max} \sim 20 - 35 \text{ km s}^{-1}$  fit the data better, whereas models with  $V_{\max} \gtrsim 40 \text{ km s}^{-1}$  are at least at the  $3\sigma$  level from the best fit values. If the initial central density slopes of the simulated subhalos were steeper than the ones adopted here, even lower values of  $V_{\max}$  would be required to fit the data. Tidal interactions do not provide the mechanism for embedding the luminous dwarf galaxies of the Milky Way within the most massive subhalos in a  $\Lambda$ CDM universe, and, therefore, for reconciling the overabundance of Galactic satellites with CDM predictions.
5. Models with a mild tangential anisotropy of stellar orbits reproduce better the shape of the observed velocity dispersion profiles of both Fornax and Draco, whereas radially anisotropic models overestimate the central stellar velocity dispersion by a factor of  $\sim 2$ . Such a tangential anisotropy is expected in scenarios in which the dSphs result from the tidal stirring of systems similar to present-day dwarf irregular galaxies.

We would like to thank the referee, Fabio Governato, for constructive comments on the manuscript and Francisco Prada for organizing the La Palma Cosmology Conference "Satellites and Tidal Streams" (2003) which motivated some of this work. Stimulating discussions with Andrey Kravtsov and Simon White are acknowledged. We are also grateful to Rocco Piffaretti for assistance with the statistical analysis and to the Swiss Center for Scientific Computing (CSCS), where the generation of the initial conditions for the cosmological runs was performed. The numerical simulations were carried out on the zBox super-computer<sup>2</sup> and on LeMieux at the Pittsburgh Supercomputing Center.

<sup>2</sup> See <http://www-theorie.physik.unizh.ch/~stadel/>

## REFERENCES

- Avila-Reese, V., Colín, P., Valenzuela, O., D'Onghia, E., & Firmani, C. 2001, *ApJ*, 559, 516
- Bahcall, N. A., et al. 2003, *ApJ*, 585, 182
- Benson, A. J., Lacey, C. G., Baugh, C. M., Cole, S., & Frenk, C. S. 2002a, *MNRAS*, 333, 156B
- Benson, A. J., Frenk, C. S., Lacey, C. G., Baugh, C. M., & Cole, S. 2002b, *MNRAS*, 333, 177B
- Bergström, L., Ullio, P., Buckley, J. H., 1998, *Astroparticle Physics*, 9, 137
- Bertschinger, E. 2001, *ApJS*, 137, 1
- Binney, J., & Mamon, G. A. 1982, *MNRAS*, 200, 361
- Binney, J., & Tremaine, S. 1987, *Galactic Dynamics* (Princeton: Princeton University Press)
- Binney, J., & Evans, N. W. 2001, *MNRAS*, 327, L27
- Blumenthal, G. R., Faber, S. M., Flores, R., & Primack, J. R. 1986, *ApJ*, 301, 27
- Bode, P., Ostriker, J. P., & Turok, N. 2001, *ApJ*, 556, 93
- Boehm, C., Riazuelo, A., Hansen, S. H., & Schaeffer, R. 2002, *Phys. Rev. D*, 66, 083505
- Bullock, J. S., Kravtsov, A. V., & Weinberg, D. H. 2000, *ApJ*, 539, 517
- . 2001, *ApJ*, 548, 33
- Bullock, J. S., Kolatt, T. S., Sigad, Y., Somerville, R. S., Kravtsov, A. V., Klypin, A., Primack, J. R., & Dekel, A. 2001a, *MNRAS*, 321, 559
- Bullock, J. S., Dekel, A., Kolatt, T. S., Kravtsov, A. V., Klypin, A. A., Porciani, C., & Primack, J. R. 2001b, *ApJ*, 555, 240
- Burkert, A. 1995, *ApJ*, 447, L25
- Calcáneo-Roldán, C., & Moore, B. 2000, *Phys. Rev. D*, 62, 123005
- Colín, P., Klypin, A., Valenzuela, O., & Gottlöber, S. 2003, *ApJ*, submitted (astro-ph/0308348)
- Croft, R. A. C., Weinberg, D. H., Bolte, M., Burles, S., Hernquist, L., Katz, N., Kirman, D., & Tytler, D. 2002, *ApJ*, 581, 20
- Debattista, V. P., & Sellwood, J. A. 2000, *ApJ*, 543, 704
- de Blok, W. J. G., McGaugh, S. S., Bosma, A., & Rubin, V. C. 2001, *ApJ*, 552, L23
- de Blok, W. J. G., McGaugh, S. S., & Rubin, V. C. 2001, *AJ*, 122, 2396
- de Blok, W. J. G., & Bosma, A. 2002, *A&A*, 385, 816
- Diemand, J., Moore, B., Stadel, J., & Kazantzidis, S. 2004, *MNRAS*, 348, 977
- Diemand, J., Moore, B., Stadel, J. 2004, *MNRAS*, in press
- Eke, V. R., Cole, S., Frenk, C. S. 1996, *MNRAS*, 282, 263
- Eke, V. R., Navarro, J. F., & Steinmetz, M. 2001, *ApJ*, 554, 114
- Fall, S. M., & Efstathiou, G. 1980, *MNRAS*, 193, 189
- Flores, R. A., & Primack, J. R. 1994, *ApJ*, 427, L1
- Gardner, J. P. 2001, *ApJ*, 557, 616
- Geha, M., Guhathakurta, P., & van der Marel, R. P. 2002, *AJ*, 124, 3073
- Ghigna, S., Moore, B., Governato, F., Lake, G., Quinn, T., & Stadel, J. 1998, *MNRAS*, 300, 146
- Gnedin, O. Y., Hernquist, L., & Ostriker, J. P. 1999, *ApJ*, 514, 109
- Hamilton, A. J. S., & Tegmark, M. 2002, *MNRAS*, 330, 506
- Hayashi, E., Navarro, J. F., Taylor, J. E., Stadel, J., & Quinn, T. 2003, *ApJ*, 584, 541 (H03)
- Jaffe, A. H., et al. 2001, *Phys. Rev. Lett.*, 86, 3475
- Kamionkowski, M., & Liddle, A. 2000, *Phys. Rev. Lett.*, 84, 4525
- Kauffmann, G., White, S. D. M., & Guiderdoni, B. 1993, *MNRAS*, 264, 201
- Kazantzidis, S., Magorrian, J., & Moore, B. 2004, *ApJ*, 601, 37
- King, I. 1962, *AJ*, 67, 471
- Klessen, R. S., Grebel, E., & Harbeck, D. 2003, *ApJ*, 589, 798
- Kleyna, J., Wilkinson, M. I., Evans, N. W., Gilmore, G., & Frayn, C. 2002, *MNRAS*, 330, 792
- Klypin, A., Kravtsov, A. V., Valenzuela, O., & Prada, F. 1999, *ApJ*, 522, 82
- Klypin, A., Zhao, H., & Somerville, R. S. 2002, *ApJ*, 573, 597
- Kochanek, C. S. 1996, *ApJ*, 457, 228
- Kravtsov, A. V., Gnedin, O. Y., & Klypin, A. 2004, *ApJ*, in press (astro-ph/0401088)
- Lemson, G., & Kauffmann, G. 1999, *MNRAS*, 302, 111
- Lin, D. N. C., Jones, B. F., & Klemola, A. R. 1995, *ApJ*, 439, 652
- Lokas, E. L. 2002, *MNRAS*, 333, 697L
- McGaugh, S. S., & de Blok, W. J. G. 1998, *ApJ*, 499, 41
- McGaugh, S. S., Barker, M. K., & de Blok, W. J. G. 2003, *ApJ*, 584, 566
- Mateo, M. 1998, *ARA&A*, 36, 435
- Mayer, L., Governato, F., Colpi, M., Moore, B., Quinn, T., Wadsley, J., Stadel, J., & Lake, G. 2001a, *ApJ*, 547, L123
- . 2001b, *ApJ*, 559, 754
- Mayer, L., Moore, B., Quinn, T., Governato, F., & Stadel, J. 2002, *MNRAS*, 336, 119



- Mayer, L., & Wadsley, J. 2003, in the Proceedings of the Conference “Satellite and Tidal Streams”, La Palma 26-30 May 2003, Spain, ed. F. Prada, D. Martínez-Delgado, & T. Mahoney (astro-ph/0309073)
- Mayer, L., & Moore, B. 2003, MNRAS, submitted (astro-ph/0309500)
- Mo, H. J., Mao, S., & White, S. D. M. 1998, MNRAS, 295, 319
- Moore, B. 1994, Nature, 370, 629
- Moore, B., Katz, N., & Lake, G. 1996, ApJ, 457, 455
- Moore, B., Ghigna, S., Governato, F., Lake, G., Quinn, T., Stadel, J., & Tozzi, P. 1999, ApJ, 524, L19
- Moore, B., Calcáneo-Roldán, C., Stadel, J., Quinn, T., Lake, G., Sebastiano, G., & Governato, F. 2001, Phys. Rev. D, 64, 063508
- Navarro, J. F., Frenk, C. S., & White, S. D. M. 1996, ApJ, 462, 563
- Odenkirchen, M., et al. 2001, AJ, 122, 2538
- Percival, W. J., et al. 2001, MNRAS, 327, 1297
- Phillips, J., Weinberg, D. H., Croft, R. A. C., Hernquist, L., Katz, N., & Pettini, M. 2001, ApJ, 560, 15
- Piatek, S., Pryor, C., Armandroff, T. E., & Olszewski, E. W. 2002, AJ, 123, 2511
- Rhee, G., Klypin, A., & Valenzuela, O. 2003, ApJ, submitted (astro-ph/0311020)
- Sand, D. J., Treu, T., & Ellis, R. S. 2002, ApJ, 574, L129
- Sand, D. J., Treu, T., Smith, G. P., & Ellis, R. S. 2004, ApJ, 604, 88
- Sellwood, J. A. 2003, ApJ, 587, 638
- Sigurdson, K., & Kamionkowski, M. 2003, Phys. Rev. Lett., submitted (astro-ph/0311486)
- Simon, J. D., Bolatto, A. D., Leroy, A., & Blitz, L. 2003, ApJ, 596, 957
- Spergel, D. N., & Steinhardt, P. J. 2000, Phys. Rev. Lett., 84, 3760
- Spergel, D. N., et al. 2003, ApJS, 148, 175
- Stadel, J. 2001, PhD thesis, University of Washington
- Stoehr, F., White, S. D. M., Tormen, G., & Springel, V. 2002, MNRAS, 335, L84 (S02)
- Stoehr, F., White, S. D. M., Springel, V., Tormen, G., & Yoshida, N. 2003, MNRAS, 345, 1313
- Susa, H., & Umemura, M. 2004, ApJ, 600, 1
- Taffoni, G., Mayer, L., Colpi, M., & Governato, F. 2003, MNRAS, 341, 434
- Tonry, J. L., et al. 2003, ApJ, 594, 1
- Tormen, G., Diaferio, A., & Syer, D. 1998, MNRAS, 299, 728
- Valenzuela, O., & Klypin, A. 2003, MNRAS, 345, 406
- Warren, M. S., Quinn, P. J., Salmon, J. K., & Zurek, W. H. 1992, ApJ, 399, 405
- Wechsler, R. H., Bullock, J. S., Primack, J. R., Kravtsov, A. V., & Dekel, A. 2002, ApJ, 568, 52
- Weinberg, M. D. 1995, ApJ, 455, L31
- Weinberg, M. D., & Katz, N. 2002, ApJ, 580, 627
- Weiner, B. J., Sellwood, J. A., & Williams, T. B. 2001, ApJ, 546, 931
- Zentner, A. R., & Bullock, J. S. 2002, Phys. Rev. D, 66, 043003
- . 2003, ApJ, 598, 49